Progress In Electromagnetics Research, Vol. 117, 479–494, 2011

NEAR-FIELD AND PARTICLE SIZE EFFECTS IN COHERENT RAMAN SCATTERING

C. H. Raymond Ooi *

Department of Physics, University of Malaya, Kuala Lumpur 50603, Malaysia

Abstract—Nonlinear optical processes have been used for sensitive detection of chemicals, optical imaging and spectral analysis of small particles. We have developed an exact theoretical framework to study the angular dependence of coherent anti-Stokes Raman scattering (CARS) intensity in the near field and far field for nanoparticle and microparticle. We obtain exact analytical solution for the CARS signal valid for arbitrary detection distance. Interesting angular dependence is found for nanoparticle, especially with near field detection. The study includes the effects of focused lasers and particle size on the CARS intensity distribution. We find that the detection distance and particle size do not affect the spectroscopic peaks of CARS. However, interference of reflected waves in nanoparticle can produce a dip in the backscattered spectrum.

1. INTRODUCTION

The CARS process [1, 2] has been used for developing a versatile real-time detection technique in spectroscopy and microscopy [3]. In particularly, backscattered ultra-violet CARS incorporated on LIDAR system [4] is promising for remote detection of molecular species present in hazardous biological aerosols [5, 6]. In practice, the aerosols could be of any shape and size ranging from micrometers to nanometers. Near field detection has been an important approach to high resolution optical microscopy [7]. Thus, it is useful to study the emission properties of the CARS technique for reliable detection of chemicals in micro- and nano-particles in the near-field regime.

Received 12 May 2011, Accepted 10 June 2011, Scheduled 18 June 2011

* Corresponding author: C. H. Raymond Ooi (rooi@um.edu.my).

We have developed an integral scattering approach combined with nonlinear microscopic theory that can describe the CARS spectra for a particle composed of a collection of complex molecules [8] as well as simple few levels quantum systems [4]. The theory provides useful results on the CARS intensity for different field components in the far field at any observation angle and for any profile of laser pulses [8].

In this paper, we study the spatial/angular dependence of coherent anti-Stokes Raman scattering (CARS) intensity and spectra for a spherical particle with different sizes. We use a nonlinear theory which goes beyond that of simple systems like dipole antenna [9]. Here, we focus on the near-field for particle composed of molecules modelled by simple few energy levels (see Fig. 1). The near field effect is interesting and was found also in emission from semiconductor quantum well [10]. Effects of the detection distance and particle size are analyzed. We compute the integral expression for the nonlinearly generated CARS signal exactly by including the $\nabla\nabla$ term exactly without making any approximation. This enables us to obtain results on the angular dependence of the CARS in the near-field regime, for the first time. We also analyze to what extend the size of the particle and the tightly focused laser pulses affect the backscattered light. Several new effects and scattering features are found and discussed, providing potential application as nano-sensor in near-field spectroscopy and imaging, and further extension to an array of nanospheres. Since we want to determine the factors that can change the spectrum, resonant or quasi-resonant states is necessary to display the resonant peaks. Off-resonant fields would not produce significant quantum coherence and well resolved peaks.

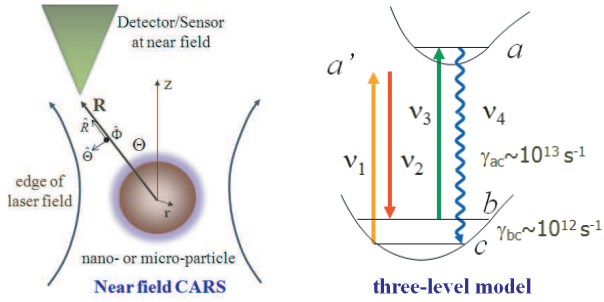

Figure 1. Configuration of near-field CARS on nanosphere with focused laser pulses. Also shown are the typical transitions in molecules modelled by three-level scheme.

2. INTEGRAL FORM OF THE SCATTERED FIELD

The physical process of interest in the nonlinear scattering by a particle can be described by the CARS (anti-Stokes) signal $\mathbf{E}$. The field dynamics is for inhomogeneous and non-magnetic medium with no free charge and no free current is described by

$$\left(\nabla^2 - \frac{1}{c^2}\frac{\partial^2}{\partial t^2}\right)\mathbf{E}(\mathbf{R},t) = -\frac{1}{\varepsilon_o}\left\{\nabla\nabla\cdot - \frac{1}{c^2}\frac{\partial^2}{\partial t^2}\right\}\mathbf{P}(\mathbf{R},t) \tag{1}$$

which gives the electric field at any time t and space $\mathbf{R}$ outside the source due to the polarization $\mathbf{P}$. In frequency space $\tilde{\mathbf{P}}(\mathbf{R},\omega) = \varepsilon_o\chi^{(1)}(\omega)\tilde{\mathbf{E}}(\mathbf{R},\omega) + \tilde{\mathbf{P}}^{NL}(\mathbf{R},\omega)$ and Eq. (1) becomes

$$\left(\nabla^2 + \frac{\omega^2}{c^2}\right)\tilde{\mathbf{E}}(\mathbf{R},\omega) = -\frac{1}{\varepsilon_o}\left\{\nabla\nabla\cdot + \frac{\omega^2}{c^2}\right\}\mathbf{P}(\mathbf{R},\omega) \tag{2}$$

with the solution

$$\tilde{\mathbf{E}}(\mathbf{R},\omega) = \left\{\nabla\nabla\cdot + k(\omega)^2\right\}\int_V \frac{\tilde{\mathbf{P}}^{NL}(\mathbf{r},\omega)e^{ik(\omega)|\mathbf{R}-\mathbf{r}|}}{4\pi\varepsilon_o|\mathbf{R}-\mathbf{r}|}d^3r \tag{3}$$

where $k(\omega) = \frac{\omega}{c}\sqrt{\varepsilon(\omega)}$, $\varepsilon(\omega) = 1+\chi(\omega)^{(e)}$ includes the local field effect $\chi^{(e)}(\omega) = \frac{\eta\alpha/\varepsilon_o}{1-\frac{\eta\alpha}{3\varepsilon_o}} = \frac{\eta\alpha/\varepsilon_o}{1-\frac{\epsilon_r-1}{\epsilon_r+2}} = \frac{\eta\alpha/\varepsilon_o}{3}(\chi^{(1)}(\omega)+3)$, α is the polarizability and $\chi^{(1)}(\omega) = \epsilon_r(\omega)-1$ is the linear susceptibility without the local field correction. Note that Eq. (3) implicitly includes the linear response. The ∇ acts on the observation coordinates $\mathbf{R}$ outside the integration volume V of the scattering medium.

The nonlinear polarization in spherical polar coordinates can be written as $\tilde{\mathbf{P}}^{NL}(\mathbf{r},\omega) = \sum_j \wp_{ca}^{(j)}\tilde{\rho}_{ac}^{(3)}(\mathbf{r}_j,\omega)\delta(\mathbf{r}-\mathbf{r}_j) = \hat{R}\tilde{P}_R^{NL} + \hat{\Theta}\tilde{P}_\Theta^{NL} + \hat{\Phi}\tilde{P}_\Phi^{NL}$ where $\tilde{P}_R^{NL} = \hat{R}\cdot\mathbf{P}^{NL}$, $\tilde{P}_\Theta^{NL} = \hat{\Theta}\cdot\mathbf{P}^{NL}$ and $\tilde{P}_\Phi^{NL} = \hat{\Phi}\cdot\mathbf{P}^{NL}$ with the unit vectors $\hat{R}$=$(\sin\Theta\cos\Phi, \sin\Theta\sin\Phi, \cos\Theta)$, $\hat{\Theta} = (\cos\Theta\cos\Phi, \cos\Theta\sin\Phi, -\sin\Theta)$ and $\hat{\Phi} = (-\sin\Phi, \cos\Phi, 0)$. The relationship with density matrix element is

$$\tilde{\mathbf{P}}^{NL}(\mathbf{r},\omega) = \eta\wp_{ca}\tilde{\rho}_{ac}^{(3)}(\mathbf{r},\omega) \tag{4}$$

where we use $\sum_j \to \eta\int_{V'} d^3r_j$ for a large number of molecules with each molecule has the same dipole moment, with a homogeneous number density η in a volume V. The coherence $\bar{\rho}_{ac}$ is obtained from the density matrix equations and Eq. (A3) in the Appendix as

$$\tilde{\rho}_{ac}^{(3)}(\mathbf{r},\omega) = \frac{i\Omega_1(\mathbf{r})\Omega_2^*(\mathbf{r})\Omega_3(\mathbf{r})\left[\frac{w_{cc}^0}{\Gamma_{a'c}^*(\omega-D)} + \frac{w_{bb}^0}{\Gamma_{a'b}(\omega-D)}\right]}{(\gamma_{ac} - i(\omega-\omega_{ac}))\left[\Gamma_{bc}^*(\omega-D) + \frac{|\Omega_2(\mathbf{r})|^2}{\Gamma_{a'c}^*(\omega-D)} + \frac{|\Omega_1(\mathbf{r})|^2}{\Gamma_{a'b}(\omega-D)}\right]} \tag{5}$$

where $D = \nu_1 - \nu_2 + \nu_3 - \omega_{bc} = \Delta_1 - \Delta_2 + \nu_3$, $\Delta_1 = \nu_1 - \omega_{ac}$, $\Delta_2 = \nu_2 - \omega_{ab}$ and $\Gamma_{a'c} = \gamma_{a'c} + i\Delta_1$, $\Gamma_{a'b} = \gamma_{a'b} + i\Delta_2$, $\Gamma_{bc} = \gamma_{bc} + i(\Delta_2 - \Delta_1)$. The inversions are $w_{a'b} = \rho_{a'a'} - \rho_{bb}$ and $w_{a'c} = \rho_{a'a'} - \rho_{cc}$. The denominator of $\tilde{\rho}_{ac}^{(3)}$ gives the saturation of the coherence $\tilde{\rho}_{bc}^{(3)}$ when the laser fields become arbitrarily large. For strong field the spectrum may be affected by the focusing of the laser fields through the $\Omega_{1,2}(\mathbf{r}) = \wp \cdot \mathbf{E}_{1,2}(\mathbf{r})/\hbar$ in the denominator. The physical explanation of how collinear lasers can satisfy the phase matching condition has been given in ref. [4].

The linear polarization is smaller than the nonlinear polarization for strong laser fields such that the nonlinear processes (especially CARS) dominate

$$\tilde{\mathbf{E}}(\mathbf{R},\omega) = \frac{\eta}{4\pi\varepsilon_o}\left[\nabla\nabla\cdot\wp_{ca} + \frac{\omega^2}{c^2}\wp_{ca}\right]\times\int_V \frac{e^{ik(\omega)\Re(\mathbf{R},\mathbf{r})}}{\Re(\mathbf{R},\mathbf{r})}\tilde{\rho}_{ac}^{(3)}(\mathbf{r},\omega)d^3r \quad (6)$$

where $\wp_{ca} = \hat{R}\wp_{ca,R} + \hat{\Theta}\wp_{ca,\Theta} + \hat{\Phi}\wp_{ca,\Phi}$ and $|\mathbf{R}-\mathbf{r}| = \Re(\mathbf{R},\mathbf{r}) = \sqrt{(X-x)^2+(Y-y)^2+(Z-z)^2}$ with $X = R\sin\Theta\cos\Phi$, $Y = R\sin\Theta\sin\Phi$, $Z = R\cos\Theta$, $x = r\sin\theta\cos\varphi$, $y = r\sin\theta\sin\varphi$ and $z = r\sin\theta$. Note that $\hat{R}(\hat{R}\cdot\wp_{ca}) + \hat{\Theta}(\hat{\Theta}\cdot\wp_{ca}) + \hat{\Phi}(\hat{\Phi}\cdot\wp_{ca}) = \wp_{ca}$ with $(\wp_{\hat{R}}, \wp_{\hat{\Theta}}, \wp_{\hat{\Phi}}) = (\hat{R},\hat{\Theta},\hat{\Phi})\cdot\wp_{ca}$. We may rewrite the integral as

$$\tilde{\mathbf{E}}(\mathbf{R},\omega) = \frac{\eta}{4\pi\varepsilon_o}\int_V\left[\mathbf{W}(\mathbf{R},\mathbf{r},\omega) + \frac{\omega^2}{c^2}\wp_{ca}F(\mathbf{R},\mathbf{r},\omega)\right]\tilde{\rho}_{ac}^{(3)}(\mathbf{r},\omega)d^3r \quad (7)$$

where $F(\mathbf{R},\mathbf{r},\omega) = \frac{e^{ik(\omega)\Re}}{\Re}$ and $\mathbf{W}(\mathbf{R},\mathbf{r},\omega)$ is defined below. Since we are focusing on the near-field effect, it is sufficiently good to use the analytical expression of Eq. (A2) in the Appendix for the coherence rather than exact numerical solutions.

Here, we obtain results that are valid for arbitrary distance without making the far field approximation. The main problem is the exact evaluation of $\mathbf{W}(\mathbf{R},\mathbf{r},\omega)$. In spherical coordinates, the $\hat{R}$, $\hat{\Theta}$, $\hat{\Phi}$ components are

$$\begin{aligned}\mathbf{W}(\mathbf{R},\mathbf{r},\omega) &= \nabla\nabla\cdot(\wp_{ca}F)\\ &= \begin{pmatrix} \frac{\partial^2 G_{\hat{R}}}{\partial R^2} + \frac{1}{R}\left(\frac{\partial}{\partial R} - \frac{1}{R}\right)\frac{\partial G_{\hat{\Theta}}}{\partial\Theta} + \frac{1}{R\sin\Theta}\left(\frac{\partial}{\partial R} - \frac{1}{R}\right)\frac{\partial G_{\hat{\Phi}}}{\partial\Phi} \\ \frac{1}{R}\frac{\partial}{\partial\Theta}\frac{\partial G_{\hat{R}}}{\partial R} + \frac{1}{R^2}\frac{\partial^2 G_{\hat{\Theta}}}{\partial\Theta^2} + \frac{1}{R^2\sin\Theta}\left(\frac{\partial}{\partial\Theta} - \frac{\cos\Theta}{\sin\Theta}\right)\frac{\partial G_{\hat{\Phi}}}{\partial\Phi} \\ \frac{1}{R\sin\Theta}\frac{\partial}{\partial R}\frac{\partial G_{\hat{R}}}{\partial\Phi} + \frac{1}{R^2\sin\Theta}\frac{\partial}{\partial\Theta}\frac{\partial G_{\hat{\Theta}}}{\partial\Phi} + \frac{1}{R^2\sin^2\Theta}\frac{\partial^2 G_{\hat{\Phi}}}{\partial\Phi^2} \end{pmatrix} \end{aligned} \quad (8)$$

where $(G_{\hat{R}}, G_{\hat{\Theta}}, G_{\hat{\Phi}}) = \wp_{ca}F = (\wp_{\hat{R}}, \wp_{\hat{\Theta}}, \wp_{\hat{\Phi}})F$. Note that $\wp_q$ are not constants, but depend on the observation point; $\wp_{\hat{R}} = \wp_x\sin\Theta\cos\Phi + \wp_y\sin\Theta\sin\Phi + \wp_z\cos\Theta$, $\wp_{\hat{\Theta}} = \wp_x\cos\Theta\cos\Phi + \wp_y\cos\Theta\sin\Phi - \wp_z\sin\Theta$ and $\wp_{\hat{\Phi}} = -\wp_x\sin\Phi + \wp_y\cos\Phi$, giving, for example, $\frac{\partial G_q}{\partial\Phi} = \wp_q\frac{\partial F}{\partial\Phi} +$

$\frac{\partial \wp_q}{\partial \Phi} F$. Thus, the derivatives of the G components are complicated because of the dependency of the $\wp_q$ on R, Θ, Φ. The terms in Eq. (8) have been evaluated analytically after lengthy calculations.

Alternatively, the vector $\mathbf{W}$ can be computed in the Cartesian coordinates, which is much simpler, using

$$\mathbf{W}(\mathbf{R},\mathbf{r},\omega) = \begin{pmatrix} \wp_x \frac{\partial^2 F}{\partial X^2} + \wp_y \frac{\partial^2 F}{\partial X \partial Y} + \wp_z \frac{\partial^2 F}{\partial X \partial Z} \\ \wp_x \frac{\partial^2 F}{\partial Y \partial X} + \wp_y \frac{\partial^2 F}{\partial Y^2} + \wp_z \frac{\partial^2 F}{\partial Y \partial Z} \\ \wp_x \frac{\partial^2 F}{\partial Z \partial X} + \wp_y \frac{\partial^2 F}{\partial Z \partial Y} + \wp_z \frac{\partial^2 F}{\partial Z^2} \end{pmatrix} \tag{9}$$

The first and second order derivatives in Eq. (8) can be evaluated, for examples $\frac{\partial F}{\partial X} = (ik\Re - 1)(X-x)\frac{\exp(ik\Re)}{\Re^3}$, $\frac{\partial}{\partial Y}(\frac{\exp(ik\Re)}{\Re^3}) = (ik\Re - 3)(Y-y)\frac{\exp(ik\Re)}{\Re^5}$, $\frac{\partial^2 F}{\partial X^2} = (ik\Re - 1)\frac{\exp(ik\Re)}{\Re^3}[1 + (ik\Re - 3)\frac{(X-x)^2}{\Re^2}]$ and $\frac{\partial^2 F}{\partial Y \partial X} = (ik\Re - 1)(ik\Re - 3)\frac{\exp(ik\Re)}{\Re^5}(X-x)(Y-y)$. The transformation between the spherical and Cartesian components are obtained through $\begin{pmatrix} R \\ \Theta \\ \Phi \end{pmatrix} = \begin{pmatrix} \sin\Theta\cos\Phi & \sin\Theta\sin\Phi & \cos\Theta \\ \cos\Theta\cos\Phi & \cos\Theta\sin\Phi & -\sin\Theta \\ -\sin\Phi & \cos\Phi & 0 \end{pmatrix} \begin{pmatrix} X \\ Y \\ Z \end{pmatrix}$ and its inverse.

We have obtained the same results using both Eqs. (8) and (9), showing consistency and correctness. We compute the emitted fields versus space and the intensity versus Θ and ω for different ρ_o and R, for incident collinear-fields and focused fields (see Figs. 2–6 and 7).

2.1. Far Field

For the far field $|\mathbf{R} - \mathbf{r}| \simeq R\sqrt{1 - 2\frac{\mathbf{R}\cdot\mathbf{r}}{R^2}} \simeq R - \frac{\mathbf{R}\cdot\mathbf{r}}{R}$ and the integral becomes $\frac{e^{ik(\omega)R}}{R}\int_V e^{ik(\omega)\frac{\mathbf{R}\cdot\mathbf{r}}{R}}\tilde{\rho}_{ac}^{(3)}(\mathbf{r},\omega)d^3r$, so the spectrum of the intensity may depend on the direction $\frac{\mathbf{R}}{R}$ but is independent of R. The situation is different in the near field. This can be seen by taking the next higher order $\frac{\mathbf{R}\cdot\mathbf{r}}{R^2}$ so we have $|\mathbf{R}-\mathbf{r}| \simeq R - \hat{R}\cdot\mathbf{r} - \frac{(\hat{R}\cdot\mathbf{r})^2}{2R}$ where the last term gives the distance and angular dependencies of the spectrum on R when R is in the order of ρ_o. We may use $|\mathbf{R}-\mathbf{r}| \simeq R - \hat{R}\cdot\mathbf{r}$ to write [4]

$$\nabla\nabla\cdot\left\{\frac{e^{ik(\omega)\Re}}{\Re}\tilde{\mathbf{P}}^{NL}(\mathbf{r},\omega)\right\} \simeq -\frac{\hat{R}}{R}k(\omega)^2\tilde{P}_R^{NL}e^{ik(\omega)(R-\hat{R}\cdot\mathbf{r})} \tag{10}$$

which gives zero radial component of the CARS field ($\nabla\nabla\cdot\wp_{ca} + \frac{\omega^2}{c^2}\hat{R}(\hat{R}\cdot\wp_{ca})$). In order to verify this analytically, we write the R component

of the [...] in Eq. (7) as

$$\left(\frac{\partial}{\partial R}+i\frac{\omega}{c}\right)\left(\frac{\partial}{\partial R}-i\frac{\omega}{c}\right)G_{\hat{R}}+\frac{1}{R}\left(\frac{\partial}{\partial R}-\frac{1}{R}\right)\left(\frac{\partial G_{\hat{\Theta}}}{\partial\Theta}+\frac{1}{\sin\Theta}\frac{\partial G_{\hat{\Phi}}}{\partial\Phi}\right) \quad (11)$$

For large R the last term vanishes and we have the $(\frac{\partial}{\partial R}+i\frac{\omega}{c})(\frac{\partial}{\partial R}-i\frac{\omega}{c})G_{\hat{R}}=0$ or $\lim_{R\to\infty}R(\frac{\partial}{\partial R}-i\frac{\omega}{c})G_{\hat{R}}=0$ which is the Sommerfeld radiation condition [11, 12].

For a nanoparticle, the focusing effect due to particle refraction is negligible. Thus, the internal field is essentially the same as the incident field. This enables us to model the internal field more easily for the case of tightly focused incident lasers, where the spatial distribution of the field is given by [13]

$$\mathbf{E}(\rho,\varphi,z)=\begin{pmatrix} I_0+I_2\cos 2\varphi \\ I_2\sin 2\varphi \\ -2I_1\cos\varphi \end{pmatrix} \quad (12)$$

where

$$I_m=\int_0^{\alpha_{\max}}E_m(\alpha)\sqrt{\cos\alpha}\sin\alpha J_m(k\rho\sin\alpha)e^{ikz\cos\alpha}d\alpha \quad (13)$$

where $E_m(\alpha)=Eg_m(\alpha)e^{-(\sin\alpha/\sin\alpha_{\max})^2}$ with $\sin\alpha_{\max}=NA/n=w_0/f$ and $g_0(\alpha)=1+\cos\alpha, g_1(\alpha)=\sin\alpha$ and $g_2(\alpha)=1-\cos\alpha$. We use $NA=1.4,\ n=1.5$ [14].

3. RESULTS AND DISCUSSIONS

The results in Figs. 2, 4, 5, 6 show the angular plots and the spectrum for three intensity components of the CARS signal from microparticle and nanoparticle with far field and near field detections.

Based on the figures, we discuss the angular dependence, directionality and subwavelength effect of the CARS signal.

3.1. Microparticle and Far Field

Although the incident lasers are polarized along the x axis, the scattered signal has the y-component especially at $\Phi=0^\circ$ and 180° since the dipoles in the particles have random orientations and can generate field in all directions transverse to the propagation direction. Fig. 2 shows the backward signal for x and y components is about 50 times smaller than the forward, consistent with previous results [4, 8]. The z component vanishes in the forward and backward due to the transversality of the propagating field. The focusing effect of the

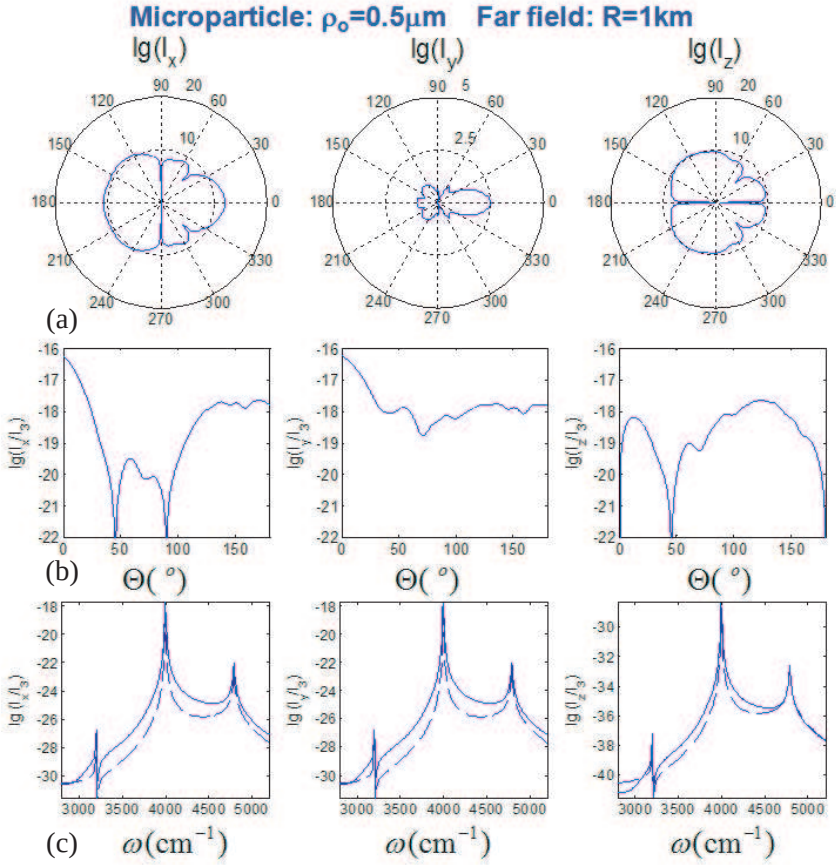

Figure 2. Far field ($R = 1\,\mathrm{km}$) CARS intensities $|E_u|^2$ ($u = x, y, z$) in log scale for microparticle ($\rho_o = 0.5\,\mu\mathrm{m}$) with collinear lasers. (a) $\lg|E_u|^2 - \min(\lg|E_u|^2)$ and (b) $\lg(|E_u|^2/|E_3|^2)$. The plots are at resonant frequency $\omega_{CARS} = \nu_1 + \nu_3 - \nu_2$. (c) The spectra are shown in log scale for forward and backward signals. The refractive indices at the carrier frequencies of the pump, Stokes, control and antiStokes fields are $n_p = 1.6, n_s = 1.7, n_c = 1.8, \sqrt{\varepsilon(\omega)} \to n_a = 1$ with $\lambda = 0.25\,\mu\mathrm{m}$ and number density $N = 9.45493 \times 10^{26}\,\mathrm{m}^{-3}$.

microparticle causes the backscattered far field intensity to be only 100 times smaller than the forward. This is in contrast to the case of bulk medium where there is no focusing effect of the lasers, where the forward intensity is typically 10^4 times larger than the backward.

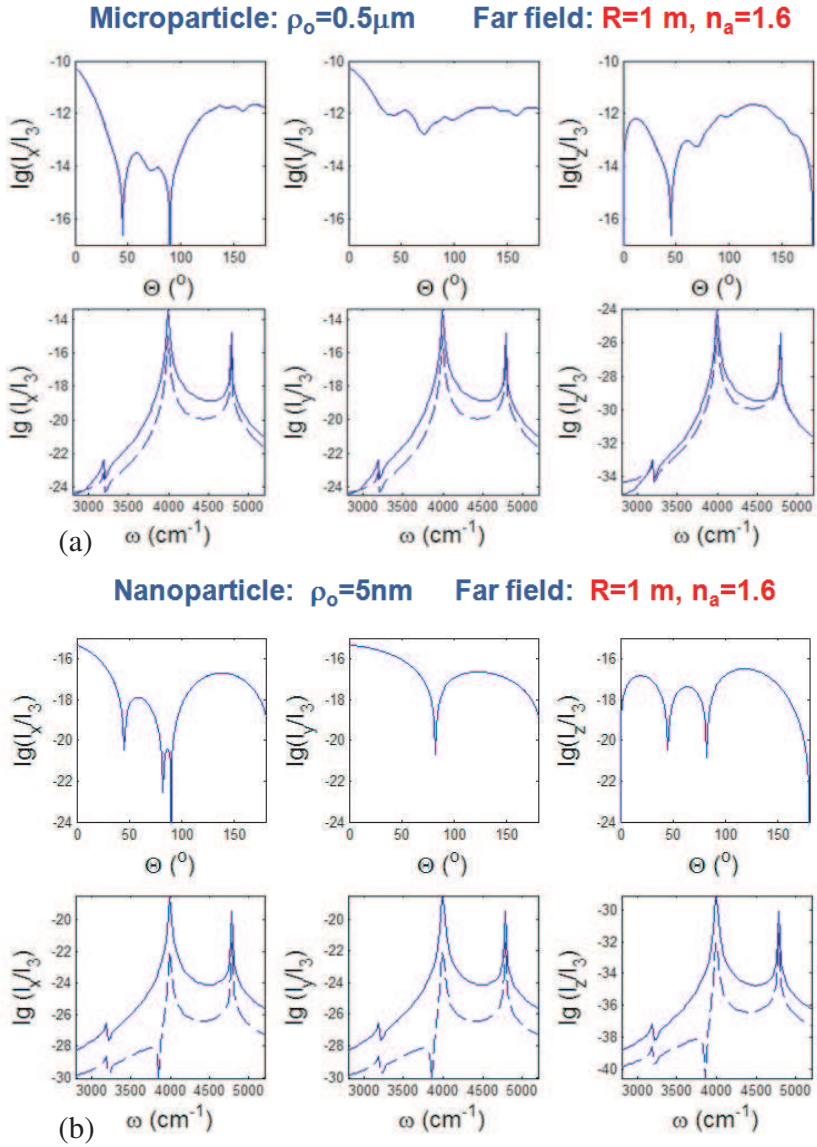

Figure 3. CARS intensities $|E_u|^2$ ($u = x, y, z$) in log scale for (a) microparticle ($\rho_o = 0.5\,\mu\text{m}$) and (b) nanoparticle ($\rho_o = 5\,\text{nm}$) at $R = 1\,\text{m}$ with $n_a = 1.6$. All other parameters are the same as in Fig. 2.

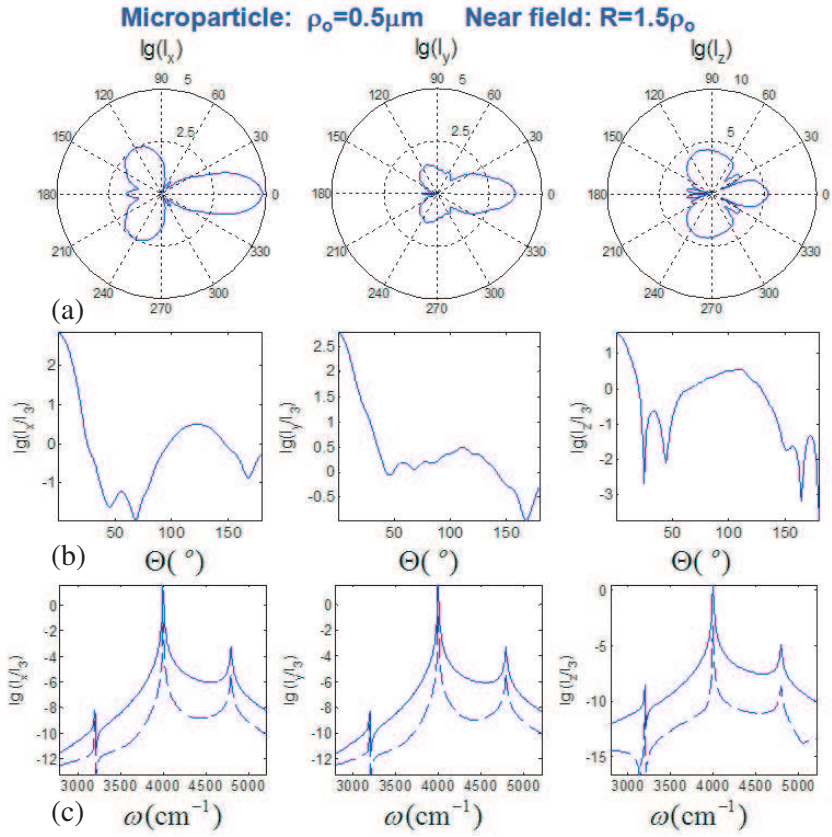

Figure 4. Near field ($R = 1.5\rho_o$) CARS intensity $|E_u|^2$ ($u = x, y, z$) in log scale for microparticle ($\rho_o = 0.5\,\mu$m) with collinear lasers. Other parameters are the same as in Fig. 2.

The strong backscattered light is mainly due to the internal reflection (about 4%) of the laser fields at the particle-air boundary. This creates reflected laser wavevectors with components in the backward direction, as if the lasers were directed in the opposite direction, which leads to the strong backscattered light. The focusing effect also creates a localized region (within $\lambda/2$ scale) with high intensity. Thus, the effective four-wave-mixing dimension is shrunk from the geometrical dimension of ρ_o down to $\lambda/2$, giving better phase matching and higher backscattered signal. At 90° detection, the x-component has a zero emission.

The intensity at $R = 1$ m is about 10^6 times larger than the

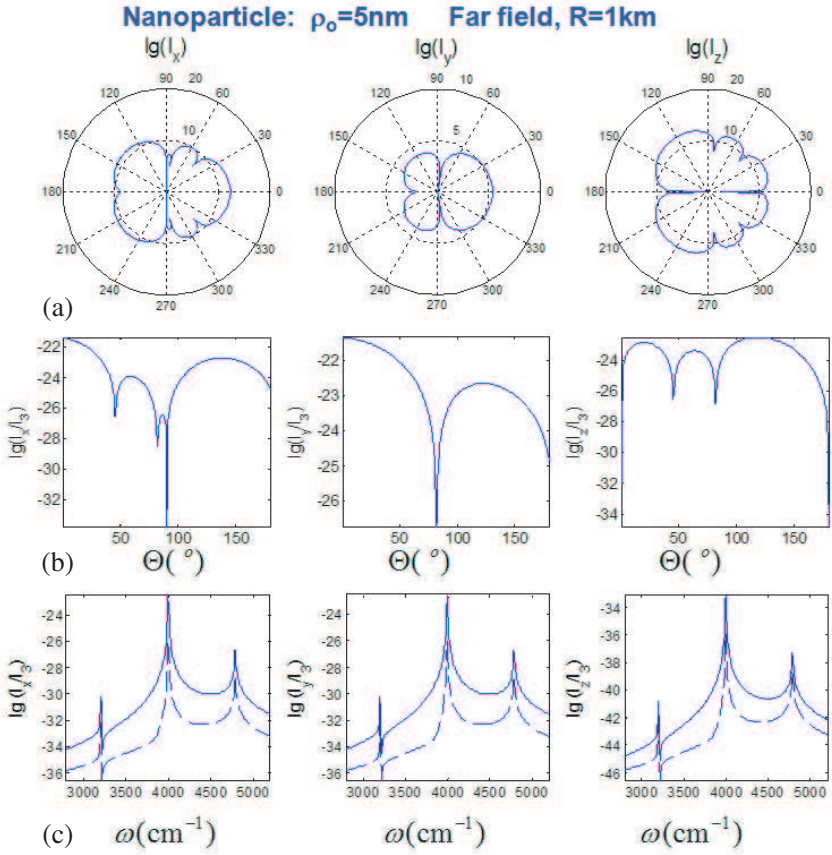

Figure 5. Far field ($R = 1\,\text{km}$) CARS intensity $|E_u|^2$ ($u = x, y, z$) in log scale for nanoparticle ($\rho_o = 5\,\text{nm}$) with collinear lasers. Other parameters are the same as in Fig. 2.

intensity at $R = 1$ km, as shown in Fig. 3. This is expected due to the inverse square law. The spectra for forward and backward detections are almost identical for $\sqrt{\varepsilon(\omega)} \to n_a = 1$, the refractive index at the antiStokes frequency. However, if the refractive index is greater than unity, i.e., $n_a = 1.6$, Fig. 3 shows that there is a "Fano-like" dip in the backward spectrum for nanoparticle. The dip is due to destructive interference of two waves reflected from the inner and outer boundaries of the nanoparticle and shifted out of phase for $n_a > 1$ but would be in phase for $n_a = 1$.

The spectrum is essentially independent of the angle of

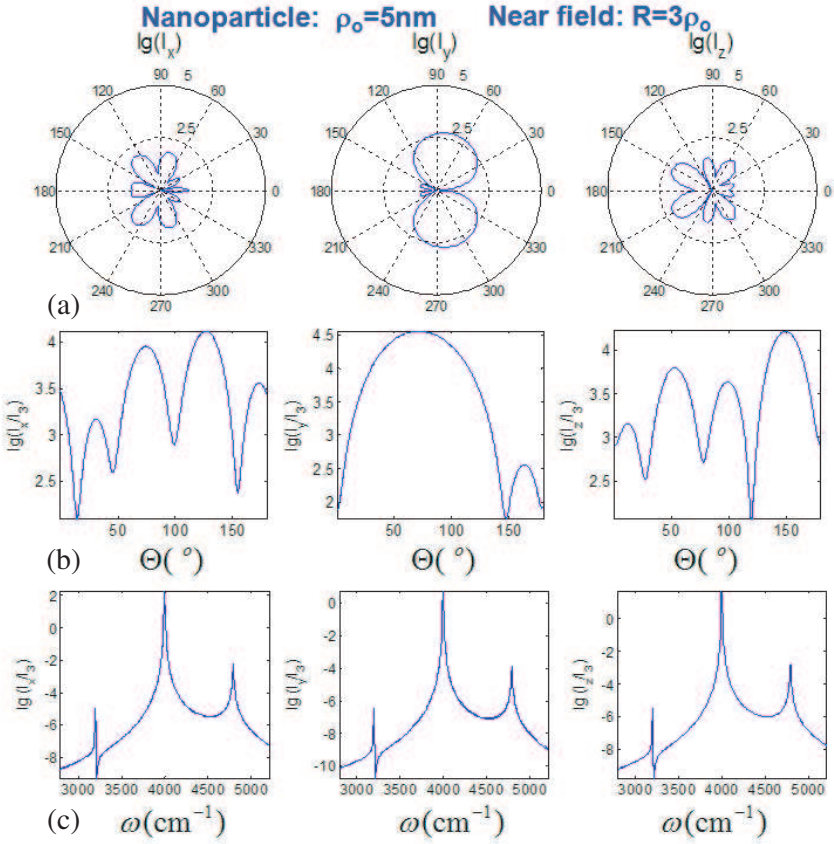

Figure 6. Near field ($R = 3\rho_o$) CARS intensity $|E_u|^2$ ($u = x, y, z$) in log scale for nanoparticle ($\rho_o = 5\,\text{nm}$) with collinear lasers. Other parameters are the same as in Fig. 2.

observation. The CARS spectrum has double dominant peaks at $\omega_{ac} = \nu_1 - \nu_2 + \nu_3 = \omega_{cars}$ and $\omega_{cars} - \omega_{bc}$. The locations of the peaks do not depend on the angle of observation.

3.2. Microparticle and Near Field

Figure 4 shows that the backward signals for the x and y components are about 1000 times smaller than the forward, which is smaller than

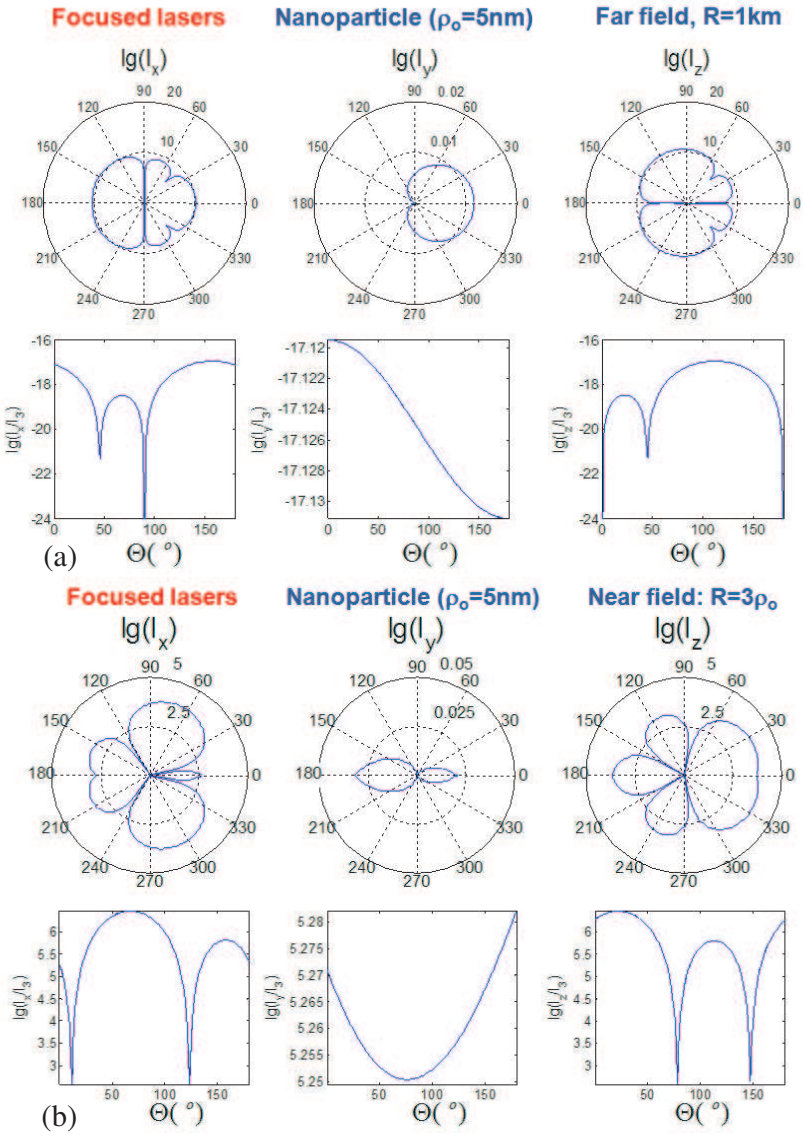

Figure 7. The CARS intensities $|E_u|^2$ $(u = x, y, z)$ in log scale for nanoparticle ($\rho_o = 5\,\text{nm}$) with tightly focused lasers. Detections are at: (a) far field ($R = 1000\,\text{m}$), (b) near field ($R = 3\rho_o$). Other parameters are the same as in Fig. 2.

the far field case. It is interesting to note the large (longitudinal) z-component in the forward, but no z-component in backward. This shows that the transversal property does not apply in the near field. At near field, there is no dip at 90°. The spectra in the near field case are essentially the same as the far field.

3.3. Nanoparticle and Far Field

For nanoparticle, Fig. 5 shows that the backward signal is only 1000 times weaker than the forward for the x component, which is still larger than bulk case. However, for the y component, the backward signal is 5000 times smaller. The y component is slightly larger than the x-component. The backscattered light is not generated by reflection as discussed above for the case of microparticle. Since the nanoparticle size is smaller than the wavelength, the focusing effect is negligible. The large signal is due to the better phase matching of the nanoparticle rather than the focusing effect. From nonlinear optics view, however, the phase matching condition is improved by the small size and not by the focusing effect, giving a strong backscattered signal. Note the zero emission or dips at 90° for the x-component but at 80° degree for the y component. The dip feature is the property of the far field, physically could be due to destructive interference. As expected, the z component is negligible for far field. Again, the spectrum is essentially unchanged.

3.4. Nanoparticle and Near Field

Some interesting results are shown in Fig. 5. The forward intensity is equal to backward for all x, y and z components. Besides, all the components have comparable strengths. Again, the z component is not negligible at the near field. The maximum intensity occurs on side observation angles, instead of in the forward or in the backward. This could be a useful asset for designing near field microscopy with off-axis detection angle. The spectrum is again essentially the same, independent of the observation angle, distance of observation (detection) and the size of the particles.

For focused lasers on the nanoparticle, Fig. 7 shows similar angular dependence, except that the intensities are higher. The forward and backward intensities for the x component are almost equal. A counter-intuitive feature is found for the near field, i.e., the backward intensity is slightly larger than the forward for the x and y components.

4. CONCLUSIONS

We have studied the effects of near field on the angular dependence of the CARS spectra. For nanoparticle with tightly focused laser fields, the backward far field is as strong as the forward. The actual advantages of the near-field are the strength and the presence of longitudinal field component in the forward direction. A possible detection system for the near field should use a probe smaller than the particle size. A narrow STM tip can be developed as a detector or sensor. The tip has a dimension close to a single atom that would be able to map out the near field distribution of the nanoparticle [15, 16]. To conclude, near-field CARS does not show subwavelength feature. The widely acclaimed subwavelength resolution in near-field microscopy is due to the proximity effect of the microscopic tip and has nothing to do with the fundamental nature of the near-field. The results of this study would be useful for designing efficient and sensitive detection systems for chemicals in small particles, including optical imaging and spectral analysis. Our study involving nonlinear process would be extended to metallic sphere [17] to study plasmonic effects. It would also be useful to apply the spectroscopic technique to combustion process by studying the effect of relativistic motion on the angular dependence of CARS using the recent formalism [18].

ACKNOWLEDGMENT

This work is supported by the University of Malaya (UM)/Ministry of Higher Education (MOHE) High Impact Research programme, the UM HIR grant No. J-00000-73588 and the MOHE FRGS grant No. FP005/2010B.

APPENDIX A. DENSITY MATRIX ELEMENTS FOR COHERENCE

We used $\frac{d}{dt}\bar{\rho}_{ac} = -\gamma_{ac}\bar{\rho}_{ac} + i\Omega_3(\mathbf{r})e^{-i\Delta_3 t}\bar{\rho}_{bc}$ which describes the transient evolution of the anti-Stokes coherence Eq. (A2) can be written as

$$\bar{\rho}^{(3)}_{ac}(\mathbf{r},t) = \int_0^t i\Omega_3(\mathbf{r},t')\bar{\rho}_{bc}(\mathbf{r},t')e^{-\Gamma_{ac}(t-t')}dt' \qquad \text{(A1)}$$

where $\Gamma_{ac} = \gamma_{ac} + i\Delta_3$, γ_{ac} is the decoherence rate. For quasi-monochromatic fields, the equation is linear and Fourier transform can

be used, giving $(\gamma_{ac} - i\omega - i\Delta_3)\mathcal{F}(\bar{\rho}_{ac}e^{i\Delta_3 t}) = i\Omega_3(\mathbf{r})\mathcal{F}(\bar{\rho}_{bc})$ or

$$\tilde{\rho}_{ac}^{(3)}(\mathbf{r},\omega) = i\Omega_3(\mathbf{r})\frac{\tilde{\rho}_{bc}^{(3)}(\mathbf{r},\omega-\nu_3+\omega_{bc})}{(\gamma_{ac} - i\omega + i\omega_{ac})} \tag{A2}$$

For monochromatic fields the ground states coherence is

$$\tilde{\rho}_{bc}(\mathbf{r},\omega-\nu_3+w_{bc}) \simeq \frac{\Omega_1(\mathbf{r})\Omega_2^*(\mathbf{r})\left[\frac{w_{a'c}}{\Gamma_{a'c}^*(\omega-D)} + \frac{w_{a'b}}{\Gamma_{a'b}(\omega-D)}\right]}{\Gamma_{bc}^*(\omega-D) + \frac{|\Omega_2(\mathbf{r})|^2}{\Gamma_{a'c}^*(\omega-D)} + \frac{|\Omega_1(\mathbf{r})|^2}{\Gamma_{a'b}(\omega-D)}}. \tag{A3}$$

where $D = \nu_1 - \nu_2 + \nu_3 - \omega_{bc} = \Delta_1 - \Delta_2 + \nu_3$, $\Delta_1 = \nu_1 - \omega_{ac}$, $\Delta_2 = \nu_2 - \omega_{ab}$ and $\Gamma_{a'c} = \gamma_{a'c} + i\Delta_1$, $\Gamma_{a'b} = \gamma_{a'b} + i\Delta_2$, $\Gamma_{bc} = \gamma_{bc} + i(\Delta_2 - \Delta_1)$. The inversions are $w_{a'b} = \rho_{a'a'} - \rho_{bb}$ and $w_{a'c} = \rho_{a'a'} - \rho_{cc}$.

REFERENCES

1. Levenson, M. D. and S. S. Kano, *Introduction of Nonlinear Spectroscopy*, Academic, San Diego, Calif., 1988.
2. Eesley, G. L., *CARS Spectroscopy*, Pergamon Press, New York, 1981.
3. Kiefer, W., "Recent advances in linear and nonlinear Raman spectroscopy I," *J. Raman Spectros*, Vol. 38, 1538, 2007.
4. Raymond Ooi, C. H., G. Beadie, G. W. Kattawar, J. F. Reintjes, Y. Rostovtsev, M. S. Zubairy, and M. O. Scully, "Theory of femtosecond coherent anti-Stokes Raman backscattering enhanced by quantum coherence for standoff detection of bacterial spores," *Phys. Rev. A*, Vol. 72, 023807, 2005.
5. Esposito, A. P., C. E. Talley, T. Huser, C. W. Hollars, C. M. Schaldach, and S. M. Lane, "Analysis of single bacterial spores by micro-Raman spectroscopy," *Appl. Spectrosc.*, Vol. 57, 868, 2003.
6. Scully, M. O., G. W. Kattawar, R. P. Lucht, T. Opatrný, H. Pilloff, A. Rebane, A. V. Sokolov, and M. S. Zubairy, "FAST CARS: Engineering a laser spectroscopic technique for rapid identification of bacterial spores," *PNAS*, Vol. 99, 10994, 2002.
7. Novotny, L., "Allowed and forbidden light in near-field optics. II. Interacting dipolar particles," *J. Opt. Soc. Am. A*, Vol. 14, 105–113, 1997.
8. Raymond Ooi, C. H., "Theory of coherent anti-Stokes Raman scattering formesoscopic particle with complex molecules: Angular-dependent spectrum," *J. Raman Spectros*, Vol. 40, 714, 2009.

9. Zhang, S., S.-X. Gong, Y. Guan, J. Ling, and B. Lu, "A new approach for synthesizing both the radiation and scattering patterns of linear dipole antenna array," *Journal of Electromagnetic Waves and Applications*, Vol. 24, No. 7, 861–870, 2010.
10. Badhane, H. P., E. P. Samuel, and D. S. Patil, "Peak optical gain at 377 nanometer and near field intensity in zinc oxide based quantum wells using electromagnetic theory," *Journal of Electromagnetic Waves and Applications*, Vol. 23, No. 2–3, 351–359, 2009.
11. Nieto-Vesperinas, M., *Scattering and Diffraction in Physical Optics*, CRC Press, 1999.
12. Rothwell, E. J., *Electromagnetics*, CRC Press, 2001.
13. Richards, B. and E. Wolf, "Structure of the image field in an aplanatic system," *Proc. R. Soc. London, Ser. A*, Vol. 253, 358, 1959.
14. Cheng, J. X., A. Volkmer, and X. S. Xie, "Theoretical and experimental characterization of coherent anti-Stokes Raman scattering microscopy," *J. Opt. Soc. Am. B*, Vol. 19, 1363, 2002.
15. Frey, H. G., S. Witt, K. Felderer, and R. Guckenberger, "High-resolution imaging of single fluorescent molecules with the optical near-field of a metal tip," *Phys. Rev. Lett.*, Vol. 93, 200801, 2004.
16. Cade, N. I., F. Culfaz, L. Eligal, T. Ritman-Meer, F.-M. Huang, F. Festy, and D. Richards, "Plasmonic enhancement of fluorescence and Raman scattering by metal nanotips," *NanoBio Technology*, Vol. 3, No. 3–4, 203–211, 2009.
17. Apostol, M. and G. Vaman, "Plasmons and diffraction of an electromagnetic plane wave by a metallic sphere," *Progress In Electromagnetics Research*, Vol. 98, 97–118, 2009.
18. Handapangoda, C. C., M. Premaratne, and P. N. Pathirana, "Plane wave scattering by a spherical dielectric particle in motion: A relativistic extension of the Mie theory," *Progress In Electromagnetics Research*, Vol. 112, 349–379, 2011.